

UniVAD: A Training-free Unified Model for Few-shot Visual Anomaly Detection

Zhaopeng Gu^{1,2} Bingke Zhu^{1,3} Guibo Zhu^{1,2}
Yingying Chen^{1,3} Ming Tang^{1,2} Jinqiao Wang^{1,2,3}

¹ Foundation Model Research Center, Institute of Automation,
Chinese Academy of Sciences, Beijing, China

² University of Chinese Academy of Sciences, Beijing, China

³ Objecteye Inc., Beijing, China

guzhaopeng2023@ia.ac.cn

{bingke.zhu, gbzhu, yingying.chen, tangm, jqwang}@nlpr.ia.ac.cn

<https://uni-vad.github.io>

Abstract

Visual Anomaly Detection (VAD) aims to identify abnormal samples in images that deviate from normal patterns, covering multiple domains, including industrial, logical, and medical fields. Due to the domain gaps between these fields, existing VAD methods are typically tailored to each domain, with specialized detection techniques and model architectures that are difficult to generalize across different domains. Moreover, even within the same domain, current VAD approaches often follow a “one-category-one-model” paradigm, requiring large amounts of normal samples to train class-specific models, resulting in poor generalizability and hindering unified evaluation across domains. To address this issue, we propose a generalized few-shot VAD method, UniVAD, capable of detecting anomalies across various domains, such as industrial, logical, and medical anomalies, with a training-free unified model. UniVAD only needs few normal samples as references during testing to detect anomalies in previously unseen objects, without training on the specific domain. Specifically, UniVAD employs a **Contextual Component Clustering** (C^3) module based on clustering and vision foundation models to segment components within the image accurately, and leverages **Component-Aware Patch Matching** (CAPM) and **Graph-Enhanced Component Modeling** (GECM) modules to detect anomalies at different semantic levels, which are aggregated to produce the final detection result. We conduct experiments on nine datasets spanning industrial, logical, and medical fields, and the results demonstrate that UniVAD achieves state-of-the-art performance in few-shot anomaly detection tasks across multiple domains, outperforming domain-specific anomaly detection models. The code will be made publicly available.

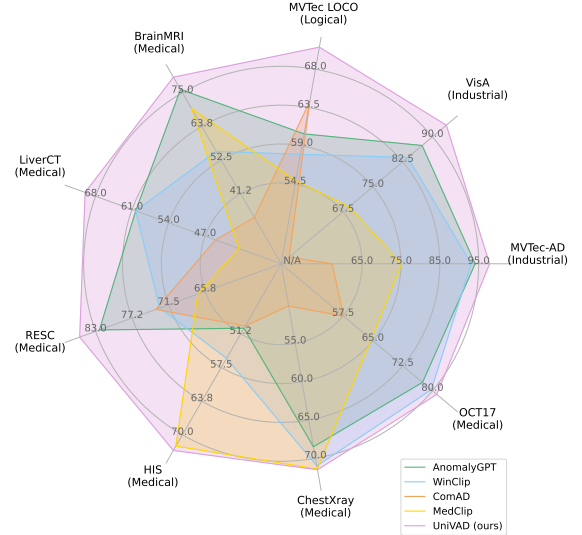


Figure 1. 1-shot performance of existing VAD methods and UniVAD across different datasets in various domains. UniVAD achieves state-of-the-art results across multiple datasets and domains, outperforming specialized methods in each domain.

1. Introduction

Visual Anomaly Detection (VAD) [11, 19, 29, 36] is a critical task that seeks to identify abnormal samples in images that deviate from established normal patterns, leveraging computer vision techniques [13, 27]. Such anomalies are rare occurrences but signify critical conditions, including errors, defects, or lesions, that necessitate timely intervention for further analysis. VAD spans multiple fields and

has applications across diverse industries, such as industrial anomaly detection [11, 19, 29], logical anomaly detection [14, 21, 25], and medical anomaly detection [2, 16].

However, significant variations in data distributions and anomaly types across domains result in current VAD methods [2, 25, 29] being highly specialized for specific domains, often employing custom detection algorithms and model architectures. Consequently, methods optimized for one domain tend to perform poorly in others. For instance, one of the state-of-the-art industrial anomaly detection methods, PatchCore [29], achieves a 1-shot image-level AUC of 84.1% on the industrial dataset MVTec-AD [4]. However, its performance drops significantly to 62.0% when applied to the MVTec LOCO [5] dataset for logical anomaly detection. Furthermore, even within the same domain, most contemporary VAD approaches adopt a “one-category-one-model” paradigm, where a separate model is trained for each object category. Once trained, each model is limited to the specific object category. This domain- and category-specific approach constrains VAD research’s standardization and scalability.

To address these limitations, we propose a training-free generalized anomaly detection method, UniVAD, which leverages a unified model to detect anomalies across multiple domains. UniVAD can handle industrial, logical, medical, and other anomalies without requiring domain-specific data training. Instead, UniVAD requires only a few normal samples of the target category during the testing phase to perform anomaly detection. This approach significantly enhances the generalizability and transferability of anomaly detection models, as illustrated in Figure 1.

Specifically, UniVAD utilizes a contextual component clustering module, incorporating clustering techniques [25] and visual foundation models [17, 22, 24] to segment components within an image. Following this, UniVAD applies a component-aware patch-matching module and a graph-enhanced component modeling module to detect anomalies at various semantic levels. The component-aware patch-matching module identifies anomalies such as structural defects or tissue lesions by matching patch-level features within each component. Meanwhile, the graph-enhanced component modeling module employs graph-based component feature aggregation to model relationships between image components, facilitating the detection of more complex logical anomalies, such as missing, added, or incorrect components, through inter-component feature matching.

Our experiments, conducted across nine datasets covering industrial, logical, and medical domains, such as MVTec-AD [4], VisA [38], MVTec LOCO [5], Brain MRI [1], and Liver CT [6, 23], demonstrate that UniVAD achieves state-of-the-art performance in few-shot anomaly detection across multiple domains, significantly outperforming domain-specific models.

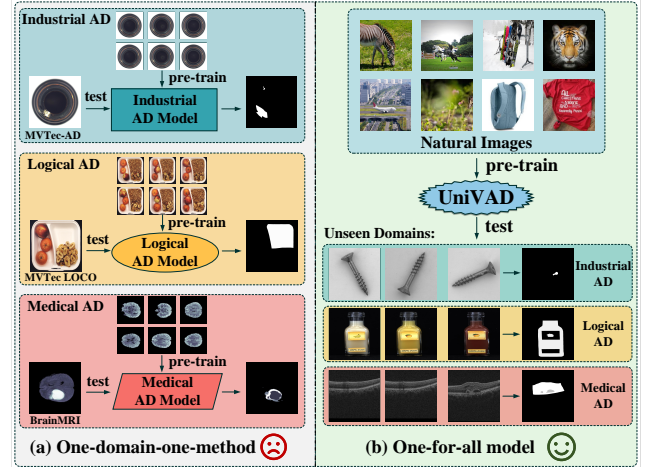


Figure 2. Comparison between UniVAD and existing VAD methods. Existing VAD methods are specifically designed for each domain, whereas UniVAD can perform anomaly detection tasks across multiple domains using a unified model.

Our contributions are listed as follows:

- We introduce the first training-free unified few-shot visual anomaly detection method capable of detecting anomalies across industrial, logical, and medical domains. This unified approach reduces the significant workload to develop separate detection methods and model architectures for each domain, thereby promoting the standardization of anomaly detection research.
- We design a contextual component clustering module that effectively segments object components under few-shot learning conditions. Additionally, combined with our component-aware patch matching module and graph-enhanced component modeling module, UniVAD reliably detects anomalies across different semantic levels.
- Comprehensive experiments on nine datasets spanning industrial, logical, and medical domains demonstrate that UniVAD achieves state-of-the-art performance in few-shot anomaly detection, establishing its effectiveness and generalizability across domains.

2. Related Work

2.1. Visual Anomaly Detection

In traditional visual anomaly detection, methods are tailored to specific domains to accommodate distinct data characteristics. Industrial anomaly detection focuses on identifying defects, which are generally small and localized, prompting recent methods to emphasize local image features. Practical approaches include patch feature matching, where patch features of test samples are compared to those of normal samples to compute anomaly scores [8, 29],

and reconstruction-based methods that leverage networks trained on normal samples to identify anomalies through reconstruction loss [18, 36]. Additionally, other approaches employ pre-trained models, such as CLIP [27], to evaluate patch features against textual descriptions of “normal” and “anomalous” states, facilitating a versatile approach to anomaly detection [10, 19].

Logical anomaly detection [5] assesses whether an image adheres to logical constraints, such as correct components, colors, or quantities, requiring a higher level of semantic understanding. Logical anomalies typically result from incorrect combinations of normal elements. Methods in this area often involve segmenting components [14, 25, 26] to evaluate individual features such as color, area, and quantity, thereby ensuring logical coherence.

Medical anomaly detection aims to locate pathological regions in medical images. Approaches in this domain include GAN-based [12], reconstruction-based [7], and self-supervised learning methods [31]. However, variability across different body parts and diseases continues to pose substantial challenges for generalizability.

Recent efforts aim to develop unified models for anomaly detection. For example, UniAD [36] employs a patch feature reconstruction method optimized for industrial applications; however, its performance decreases in other domains and requires large volumes of normal data samples for model training.

In contrast, UniVAD operates across domains using a training-free unified model and requires only a few normal samples for reference during testing, as shown in Figure 2. This approach eliminates the need for prior training on domain-specific data, offering greater flexibility across various anomaly detection tasks.

2.2. Component Segmentation

Logical anomaly detection frequently relies on component segmentation to extract sub-parts of an image and evaluate each for anomalies. ComAD [25] introduces this approach by using clustering for segmentation; however, clustering requires many samples, limiting its applicability in few-shot scenarios. More recent methods, such as CSAD [14] and SAM-LAD [26], leverage vision models like SAM [22] but face challenges with segmentation granularity, often producing outputs that are either overly fine or too coarse. PSAD [21] addresses this issue by employing a limited set of annotated samples, which increases training costs and requires manual labeling.

UniVAD combines clustering with vision foundation models, utilizing vision foundation models to produce initial component masks and refining segmentation granularity through clustering. This approach allows for precise segmentation in few-shot settings, enhancing the model’s ability to perform effectively with minimal data.

3. Method

3.1. Overall Architecture

Given a query image $I_q \in \mathbb{R}^{H \times W \times 3}$ and K reference normal images $I_n \in \mathbb{R}^{K \times H \times W \times 3}$, UniVAD first employs a contextual component clustering module to segment components within both the query and reference images, producing corresponding component masks. UniVAD then utilizes an image encoder pre-trained on large-scale datasets to extract features from the query and normal images, resulting in a feature map $F_q \in \mathbb{R}^{H_1 \times W_1 \times C}$ for the query image and $F_n \in \mathbb{R}^{K \times H_1 \times W_1 \times C}$ for the normal images. By applying group average pooling based on the component masks, UniVAD obtains component-level features for both the query and normal images, denoted as $F_{qc} \in \mathbb{R}^{N_q \times C}$ for the query image and $F_{nc} \in \mathbb{R}^{K \times N_n \times C}$ for the normal images, where N_q and N_n represent the number of components in the query and normal images, respectively.

The feature maps F_q and F_n are subsequently passed through interpolation to obtain patch-level features, $P_q \in \mathbb{R}^{H_2 \times W_2 \times C}$ and $P_n \in \mathbb{R}^{K \times H_2 \times W_2 \times C}$. In parallel, textual descriptions of normal and anomalous semantics are processed by a text encoder, yielding textual features $T_n \in \mathbb{R}^C$ for normal semantics and $T_a \in \mathbb{R}^C$ for anomalous semantics. The patch-level features P_q , P_n , and textual features T_n and T_a are then input into the component-aware patch-matching module to generate a structural anomaly map.

At the same time, the component features of query image and normal images, F_{qc} and F_{nc} , are passed through the graph-enhanced component modeling module to produce a logical anomaly map. Finally, UniVAD combines the structural and logical anomaly maps to generate the final unified anomaly detection result, as shown in Figure 3.

In Sec 3.2 to 3.4, we provide a detailed description of contextual component clustering, component-aware patch matching, and graph-enhanced component modeling. Additionally, we provide pseudo-code descriptions of these modules in Appendix A.

3.2. Contextual Component Clustering

To achieve accurate component segmentation with limited normal samples, we propose the Contextual Component Clustering (C^3) module, which combines visual foundation models with clustering techniques to enable precise component segmentation in few-shot setting.

Upon receiving an input image, the C^3 module first uses the Recognize Anything Model [37] to identify objects and generate content tags. Next, the Grounded SAM [28] method generates masks for all detected elements. However, SAM [22] often faces challenges with segmentation granularity, producing masks that are either too fine or too coarse, which can be inconsistent across normal and query images. To address this, we refine and filter SAM’s output.

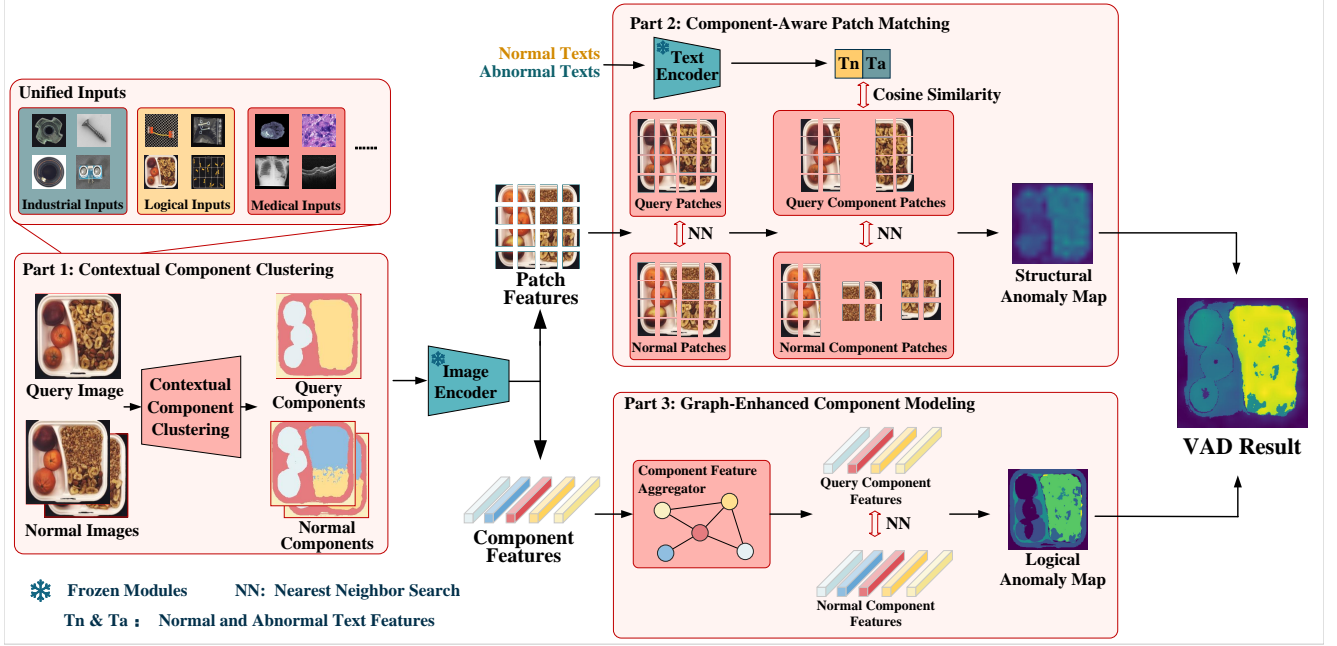


Figure 3. The overall architecture of UniVAD. Given an input image, UniVAD first generates masks for each entity using the Contextual Component Clustering module (Sec 3.2). UniVAD then applies the Component-Aware Patch Matching module (Sec 3.3) and the Graph-Enhanced Component Modeling module (Sec 3.4) to detect structural and logical anomalies. The outputs from both expert modules are combined to produce the final unified anomaly detection result.

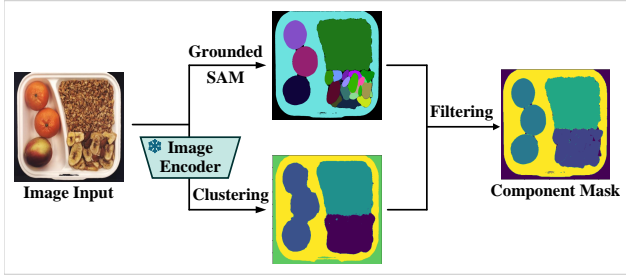


Figure 4. Architecture of the C^3 module.

Specifically, after obtaining M initial component masks from Grounded SAM, represented as $M_{\text{sam}} \in \mathbb{R}^{M \times H \times W}$, the C^3 module evaluates the masks based on their quantity and area coverage. If only one mask is generated and it covers nearly the entire image (exceeding $\gamma\%$ of the area), we infer that the image represents a textured surface (e.g., wood), and treat the entire image as a single component, outputting a mask covering the full image: $M = \mathbf{1}_{H \times W}$.

If Grounded SAM generates a single mask that covers less than $\gamma\%$ of the image area, we speculate that the image contains a single object, and we directly use the SAM-produced mask as the final mask: $M = M_{\text{sam}}$.

In cases where Grounded SAM produces multiple masks, indicating the presence of multiple objects, we refine the SAM-generated masks using a clustering approach,

as shown in Figure 4. Specifically, we first extract the feature map of the normal images $F_n \in \mathbb{R}^{K \times H_1 \times W_1 \times C}$ using a pre-trained image encoder. Then, we apply the K-means clustering algorithm to the features in F_n , clustering them into N groups and yielding N cluster centroids $C \in \mathbb{R}^{N \times C}$. For each feature in the feature maps of both normal and query images, we compute its similarity to each cluster centroid, thereby generating N cluster masks for the image, denoted as $M_{\text{cluster}} \in \mathbb{R}^{N \times H_1 \times W_1}$. After that, we filter the background masks by evaluating whether the values at the four corners of each mask are non-zero. This process yields N' valid masks, which are then resized to the original image dimensions to produce $M_{\text{valid}} \in \mathbb{R}^{N' \times H \times W}$.

Next, for each mask M_{sam}^i in M_{sam} , we compute the Intersection over Union (IoU) between M_{sam}^i and each mask in M_{valid} , identifying the mask M_{valid}^j with the highest IoU. We then assign the label j to M_{sam}^i :

$$\text{Label}(M_{\text{sam}}^i) = \arg \max_j \text{IoU}(M_{\text{sam}}^i, M_{\text{valid}}^j). \quad (1)$$

Finally, for each j ($1 \leq j \leq N'$), the C^3 module replaces the original mask M_{valid}^j with the union of the masks in M_{sam} that are assigned the label j , resulting in the final mask set $M \in \mathbb{R}^{N' \times H \times W}$:

$$M^j = \bigcup_{\text{Label}(M_{\text{sam}}^i)=j} M_{\text{sam}}^i. \quad (2)$$

This approach combines the precise segmentation capabilities of visual foundation models with the granularity control provided by clustering methods, enabling accurate component segmentation in few-shot settings.

Upon completing component segmentation, UniVAD proceeds to detect structural and logical anomalies in the image using the component-aware patch-matching module and the graph-enhanced component modeling module.

3.3. Component-Aware Patch Matching

Our Component-Aware Patch Matching (CAPM) method builds on patch feature matching, extending it by incorporating component constraints and image-text feature similarity comparisons to improve performance.

In the patch feature matching process, we first employ a network pretrained on large-scale datasets, such as ImageNet [30], as an image encoder to extract the feature map of the query image, $F_q \in \mathbb{R}^{H_1 \times W_1 \times C}$, and the feature map of the normal images, $F_n \in \mathbb{R}^{K \times H_1 \times W_1 \times C}$. Next, both F_q and F_n are processed through interpolation to obtain patch features $P_q \in \mathbb{R}^{H_2 \times W_2 \times C}$ and $P_n \in \mathbb{R}^{K \times H_2 \times W_2 \times C}$, respectively. For each patch in the query image, we compute the cosine distance between P_q^i and all patch features in P_n , using the minimum cosine distance as the patch-matching anomaly score for P_q^i , as shown in Eq. (3):

$$Score_{pm}(P_q^i) = \min(\text{distance}(P_q^i, P_n)). \quad (3)$$

However, the standard patch feature matching method encounters limitations, such as its inability to distinguish between foreground and background regions, which may lead to false positives in background areas, and its failure to differentiate between different object components, which can mistakenly pair patches from other irrelevant regions with similar color or texture, resulting in missed detections. To address these issues, we leverage the component mask obtained from the C^3 module to perform feature matching within each component, effectively enhancing the accuracy of anomaly detection.

Specifically, after obtaining the patch features P_n of normal samples, we use the N' component masks derived from the C^3 module to create N' patch subsets P_{ni} ($1 \leq i \leq N'$), where patches within each mask are allocated to their respective subsets:

$$P_{ni} = \{P_n^j \mid M_i^j = 1\}. \quad (4)$$

We apply the same process to P_q to obtain P_{qi} , and perform patch feature matching within each subset to calculate the component-aware anomaly score for each patch:

$$Score_{aware}(P_{qi}^j) = \min(\text{distance}(P_{qi}^j, P_{ni})). \quad (5)$$

Additionally, we employ an image-text feature-matching approach to calculate an anomaly score for each patch.

Specifically, we extract normal and anomalous text features, T_n and T_a , using a pretrained text encoder that encodes the textual descriptions of normal and anomalous states. We then compute the cosine similarity between each patch feature of the query image and T_n and T_a , obtaining the image-text anomaly score for each patch:

$$Score_{vl}(P_{qi}^j) = \text{softmax}(\text{sim}(P_{qi}^j, [T_n, T_a])), \quad (6)$$

where $\text{sim}(\cdot, \cdot)$ represents the cosine similarity calculation.

Finally, we sum the three anomaly scores for each patch to derive the structural anomaly score map:

$$Score_{stru} = \alpha Score_{pm} + \beta Score_{aware} + \gamma Score_{vl}, \quad (7)$$

where α , β and γ are hyperparameters, which are all set to $1/3$ in our experiments.

3.4. Graph-Enhanced Component Modeling

The CAPM module introduced earlier is primarily designed to detect structural anomalies with low-level semantics, where the anomalous content has never appeared in the normal samples. However, for higher-level semantic logical anomalies, the image content may exist in the normal samples but is combined incorrectly. Such anomalies are challenging to detect through patch feature matching alone, as they require a higher level of semantic understanding.

To address this problem, we design a Graph-Enhanced Component Modeling (GECM) module, which focuses on the holistic characteristics of each component, enabling it to detect the addition, omission, or misplacement of components. Specifically, after obtaining the component masks, the GECM module first employs a pretrained feature extractor to generate the feature map $F_q \in \mathbb{R}^{H_1 \times W_1 \times C}$ for the query image and $F_n \in \mathbb{R}^{K \times H_1 \times W_1 \times C}$ for the normal images. We then apply group average pooling to capture the deep features of each component from the query and normal samples, denoted as $F_{qc} \in \mathbb{R}^{N_q \times C}$ and $F_{nc} \in \mathbb{R}^{K \times N_n \times C}$.

Next, we employ a Component Feature Aggregator (CFA) module to further model each component's features. In the Component Feature Aggregator, we initially model each component feature as a node in a graph, and the cosine similarity between any two component features as the weight of the edge connecting these nodes, allowing us to compute the adjacency matrix for all nodes in the graph:

$$A = \begin{bmatrix} S_{11} & S_{12} & \cdots & S_{1N} \\ S_{21} & S_{22} & \cdots & S_{2N} \\ \vdots & \vdots & \ddots & \vdots \\ S_{N1} & S_{N2} & \cdots & S_{NN} \end{bmatrix}, \quad (8)$$

where N denotes the number of components (N_q for the query image and N_n for normal images), and S_{ij} represents

Table 1. Comparison between UniVAD and existing methods under the 1-normal-shot setting, where image-level AUC and pixel-level AUC are used to evaluate the performance of image-level anomaly detection and pixel-level anomaly localization, respectively. The best results are highlighted in **bold**.

Task	Dataset	PatchCore	AnomalyGPT	WINCLIP	ComAD	UniAD	MedCLIP	UniVAD (ours)
Image-level (AUC)	MVTec-AD	84.0	94.1	93.1	57.3	70.3	75.2	97.8
	VisA	74.8	87.4	83.8	53.9	61.3	69.0	93.5
	MVTec LOCO	62.0	60.4	58.0	62.2	50.9	54.9	71.0
	BrainMRI	73.2	73.1	55.4	33.3	50.0	69.7	80.2
	LiverCT	44.9	60.3	60.3	45.0	35.0	40.5	70.0
	RESC	56.3	82.4	72.9	73.5	53.5	66.9	85.5
	HIS	55.6	50.2	55.8	49.8	50.0	71.1	72.6
	ChestXray	66.4	68.5	70.2	50.1	60.6	71.4	72.2
	OCT17	59.9	77.5	79.7	57.6	44.4	64.6	82.1
Pixel-level (AUC)	MVTec-AD	89.9	95.3	95.2	-	90.7	79.1	96.5
	VisA	93.4	96.2	96.2	-	90.3	88.2	98.2
	MVTec LOCO	69.8	70.3	58.8	-	70.6	69.1	75.1
	BrainMRI	96.0	96.0	86.6	-	93.6	91.7	96.8
	LiverCT	95.6	95.8	94.5	-	88.5	93.8	96.3
	RESC	78.2	94.0	87.9	-	80.7	91.5	94.9

the normalized similarity between nodes i and j , defined as:

$$S_{ij} = \frac{S'_{ij}}{\sum_{k=1}^N S'_{ik}}, S'_{ij} = \text{sim}(\text{node}_i, \text{node}_j). \quad (9)$$

Subsequently, we leverage the adjacency matrix A to aggregate node information again via a graph attention operation, resulting in feature embeddings that more comprehensively represent the overall characteristics of each component. Specifically, these embeddings are expressed as $E_q = G(A_q, F_{qc})$ and $E_n = G(A_n, F_{nc})$, where G represents the graph attention operation [34].

For each component feature embeddings E_q^i in E_q , we compute its minimum cosine distance to the vectors in E_n , which serves as the deep anomaly score for that component:

$$\text{Score}_{\text{deep}}(E_q^i) = \min(\text{distance}(E_q^i, E_n)). \quad (10)$$

In addition to deep features, geometric features such as component area, color, and position are also effective for detecting logical anomalies. Therefore, we compute these geometric features for each component in both query and normal samples, combining them into geometric feature vectors, represented as $G_q \in \mathbb{R}^{N_q \times C_g}$ and $G_n \in \mathbb{R}^{N_n \times C_g}$, and utilize the following formula to calculate the geometric anomaly score:

$$\text{Score}_{\text{geo}}(G_q^i) = \min(\text{distance}(G_q^i, G_n)). \quad (11)$$

Then, we combine $\text{Score}_{\text{deep}}$ and $\text{Score}_{\text{geo}}$ to obtain the logical anomaly score:

$$\text{Score}_{\text{logic}} = \phi \text{Score}_{\text{deep}} + \psi \text{Score}_{\text{geo}}. \quad (12)$$

where ϕ and ψ are hyperparameters, and they are set to 0.5 in our experiments.

By combining $\text{Score}_{\text{stru}}$ and $\text{Score}_{\text{logic}}$, we derive the final anomaly score map:

$$\text{Score}_{\text{final}} = \delta \text{Score}_{\text{stru}} + \eta \text{Score}_{\text{logic}}, \quad (13)$$

where δ and η are set to 0.5 by default.

4. Experiments

4.1. Experimental Setups

Datasets. We conduct extensive experiments on nine datasets spanning industrial, logical, and medical anomaly detection domains. For industrial anomaly detection, we use the widely recognized MVTec-AD [4] and VisA [38] datasets. For logical anomaly detection, we focus on the comprehensive MVTec LOCO [5] dataset. In the medical anomaly detection domain, following the recent BMAD benchmark, we select six datasets: BrainMRI [1], liverCT [6, 23], RetinalOCT [15], ChestXray [32], HIS [3], and OCT17 [20]. Since ChestXray [32], HIS [3], and OCT17 [20] datasets do not provide pixel-level anomaly annotations, we evaluate only image-level anomaly detection performance on these three datasets. A detailed description of the nine datasets is provided in Appendix B.

Competing Methods and Baselines. In this study, we compare the performance of UniVAD with state-of-the-art methods from various domains, under two different settings, few-normal-shot and few-abnormal-shot. In the few-normal-shot setting, the model is not trained on the target dataset; instead, a few normal samples are provided only as reference during testing. Under this setting, we selected

Table 2. Comparison between UniVAD and existing methods under the 4-abnormal-shot setting, where image-level AUC and pixel-level AUC are used to evaluate the performance of image-level anomaly detection and pixel-level anomaly localization, respectively. The experimental results in the table are cited from MVFA [16], and the best results are highlighted in **bold**.

Task	Dataset	DRA	BGAD	MVFA	UniVAD
Img-level (AUC)	BrainMRI	80.6	83.6	92.4	94.1
	LiverCT	59.6	72.5	81.2	87.5
	RESC	90.9	86.2	96.2	97.3
	HIS	68.7	-	82.7	85.7
	ChestXray	75.8	-	82.0	82.4
	OCT	99.0	-	99.4	99.7
Px-level (AUC)	BrainMRI	74.8	92.7	97.3	98.6
	LiverCT	71.8	98.9	99.7	99.7
	RESC	77.3	93.8	99.0	99.0

PatchCore [29], WinCLIP [19], AnomalyGPT [11], and UniAD [36] for industrial anomaly detection, ComAD [25] for logical anomaly detection, and MedCLIP [33] for medical anomaly detection. Few-abnormal-shot is a commonly used setting in medical anomaly detection, where testing is performed after training on a small number of normal and abnormal samples from the target dataset. To demonstrate the generality of UniVAD, we also compared it with existing methods in the few-abnormal-shot setting, selecting DRA [9], BGAD [35], and MVFA [16] under this setting.

Evaluation Protocols. In alignment with established anomaly detection methodologies, we evaluate performance using the Area Under the Receiver Operating Characteristic Curve (AUC). Image-level AUC is used to assess anomaly detection performance, while pixel-level AUC is employed to evaluate anomaly localization performance.

Implementation Details. In few-normal-shot setting, we do not conduct any further training on anomaly detection datasets for UniVAD. We resize all images to a resolution of 448x448 pixels, and utilize two widely used vision encoders, CLIP-L/14@336px and DINOv2-G/14, as our image encoders, with their parameters frozen. For image-level anomaly scores, it is common to derive results from pixel-level outputs using a post-processing method. Depending on the distribution of detection data, popular approaches include using either the maximum or the mean of pixel-level results. In UniVAD, for datasets like HIS [3], where abnormal samples (*e.g.*, cancer cell-stained slides) exhibit global differences compared to normal samples, we use the mean of the pixel-level results as the image-level anomaly score. For industrial anomaly detection, logical anomaly detection, and the remaining medical anomaly detection datasets, where abnormal regions occupy only a small portion of the image and the rest remains normal, we use the maximum of pixel-level results as the global anomaly score.

Table 3. Comparison of different implementations of the C^3 module across multiple datasets. *G-SAM Only* in table refers to the use of visual foundation models exclusively. The best performance results are highlighted in **bold**.

Dataset	Cluster Only	G-SAM Only	C^3 Module
MVTec-AD	(97.3, 96.1)	(97.5, 96.1)	(97.8, 96.5)
VisA	(92.5, 98.0)	(92.1, 97.7)	(93.5, 98.0)
MVTec LOCO	(67.5, 70.9)	(67.8, 74.9)	(71.0, 75.1)
BrainMRI	(73.9, 96.7)	(74.5, 94.9)	(80.2, 96.8)
LiverCT	(63.6, 96.1)	(63.7, 96.3)	(70.0, 96.3)
RESC	(84.2, 94.9)	(85.0, 94.6)	(85.5, 94.9)

Table 4. Comparison of the clustering part in the C^3 module using image features extracted by different image encoders.

Dataset	CLIP-ViT	DINO	DINOv2
MVTec-AD	(97.7, 96.5)	(97.8, 96.5)	(97.9, 96.4)
VisA	(93.5, 98.0)	(93.5, 98.0)	(93.2, 98.0)
MVTec LOCO	(71.1, 74.5)	(71.0, 75.1)	(70.9, 74.6)
RESC	(85.2, 94.6)	(85.5, 94.9)	(85.2, 94.8)

4.2. Main Results

Few-normal-shot Setting. We conduct experiments using the same few-normal-shot setting as most existing few-shot anomaly detection methods [11, 19, 29], where the model is tested on objects it has never encountered during training, with a small number of normal samples provided as references during testing. Table 1 presents a comparison of the performance of UniVAD and various domain-specific anomaly detection methods under the 1-normal-shot setting. It can be observed that UniVAD significantly outperforms existing domain-specific methods in both image-level and pixel-level results across different domains. Compared to state-of-the-art methods in each domain, our approach achieves an average improvement of 6.2% in image-level AUC and 1.7% in pixel-level AUC. The experimental results demonstrate the strong transferability of UniVAD.

Few-abnormal-shot Setting. One of the key features of UniVAD is its robust generalization capability. Without requiring any training on domain-specific anomaly detection datasets, UniVAD demonstrates outstanding cross-domain anomaly detection performance by using only a minimal number of normal samples as a reference during the testing phase. On the other hand, for scenarios demanding high-precision detection on specific domain data, we provide a domain adaptation training method. This method allows UniVAD to be fine-tuned on domain-specific datasets to achieve optimal performance for particular tasks. Such fine-tuning requires only a small number of normal and anomalous samples from the target dataset, which is referred to as the few-abnormal-shot setting. Several popular medi-

Table 5. Comparison between Patch Matching and CAPM methods on MVTec-AD, VisA, MVTec LOCO and BrainMRI datasets. *Img-AUC* and *Px-AUC* in table represent image-level AUC and pixel-level AUC. The best performance results are in **bold**.

Dataset	Patch Matching		CAPM	
	Img-AUC	Px-AUC	Img-AUC	Px-AUC
MVTec-AD	96.9	96.3	97.8	96.5
VisA	91.8	97.8	93.4	98.2
MVTec LOCO	62.0	69.8	64.1	70.2
BrainMRI	79.1	96.4	80.2	96.8

cal anomaly detection methods [9, 16, 35] employ the few-abnormal-shot setting for experimentation. We apply the same approach to UniVAD and present a comparison of its performance with these methods under the 4-abnormal-shot setting across six medical datasets in Table 2. Experimental results indicate that, under the few-abnormal-shot setting, UniVAD also outperforms existing approaches. Implementation details about UniVAD in the few-abnormal-shot setting can be found in Appendix C.

4.3. Ablation Study

We conduct extensive ablation studies on our proposed modules to demonstrate their effectiveness. Here, we primarily present the ablation results of our core module, with additional ablation study results provided in Appendix D.

Contextual Component Clustering. Contextual Component Clustering (C^3) module is built upon visual foundation models such as RAM [37], Grounding DINO [24], and SAM [22], as well as clustering techniques. It addresses the challenges of poor performance in few-shot settings commonly encountered in clustering methods and the difficulty of controlling segmentation granularity in SAM [22]. In Table 3, we present a comparative analysis of performance results using only visual foundation models, only clustering methods, and the C^3 module, demonstrating the effectiveness of the C^3 module. We also provide a comparison of different image encoders utilized in clustering in Table 4. The performance differences are minimal, demonstrating the robustness of the C^3 module across various encoders.

Component-Aware Patch Matching. The original patch feature matching method matches all patch features from the entire image, which can mistakenly pair patches from background or other irrelevant regions with similar color or texture, leading to decreased anomaly detection performance. In contrast, the CAPM module restricts the matching regions of patch features, ensuring that source and target patches originate from the same part. Table 5 compares the performance of the original patch matching method and CAPM across multiple datasets, highlighting the effectiveness of CAPM in detecting structural anomalies.

Table 6. Comparison on the MVTec LOCO dataset under different settings. *Geo feat.* represent components geometric features, *Deep feat.* represents component deep features, and *CFA* represents component feature aggregator. The best performance results are highlighted in **bold**.

Modules in GECM			MVTec LOCO	
Geo feat.	Deep feat.	CFA	Image-AUC	Pixel-AUC
			64.1	70.2
✓			66.6	73.2
✓	✓		69.4	74.8
✓	✓	✓	71.0	75.1

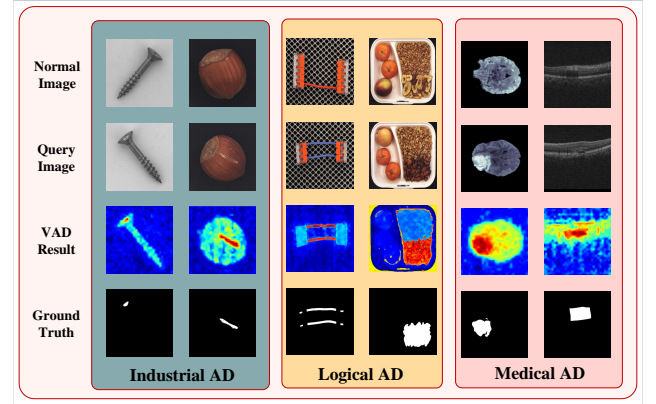


Figure 5. Visualization result of UniVAD on datasets across diverse domains. UniVAD demonstrates a strong transferability by accurately segmenting previously unseen samples with only a single normal sample provided as reference.

Graph-Enhanced Component Modeling. Patch features with low-level semantics struggle to capture the overall characteristics of each component. Our GECM method, built on a graph neural network, models the interaction between each component’s geometric and deep features, enhancing the detection performance for logical anomalies with high-level semantics. Table 6 compares the performance differences from using only CAPM to incrementally adding each module in GECM, demonstrating GECM’s notable effectiveness in detecting logical anomalies.

4.4. Visualization Results

Figure 5 illustrates the visual anomaly detection results of UniVAD across various datasets in industrial anomaly detection, logic anomaly detection, and medical anomaly detection. With only a single normal sample as a reference, UniVAD accurately detects anomalies in previously unseen items across diverse domains, demonstrating the method’s strong transferability and practical applicability.

5. Limitation

UniVAD currently relies on visual foundation models such as RAM [37], Grounding DINO [24], and SAM [22] for component segmentation. The inference time for an image is approximately 0.7 seconds, which somewhat limits its applicability in real-time scenarios. However, the key strength of UniVAD lies in its remarkable generalization capability. Even when provided with only a small number of normal samples as references, UniVAD is able to accurately detect anomalies across diverse domains, thereby advancing the standardization of anomaly detection research.

6. Conclusion

In this paper, we propose UniVAD, a novel, training-free, unified few-shot visual anomaly detection method capable of detecting anomalies across various domains, including industrial, logical, and medical fields, using a unified model. By leveraging a contextual component clustering module for precise segmentation, along with component-aware patch matching and graph-enhanced component modeling for multi-level anomaly detection, UniVAD achieves superior performance without the need for domain-specific models or extensive training data. Experimental results across multiple datasets demonstrate that UniVAD outperforms existing domain-specific approaches, offering a more flexible and scalable solution for visual anomaly detection tasks and contributing to the standardization of research in the field of visual anomaly detection.

References

- [1] Ujjwal Baid, Satyam Ghodasara, Suyash Mohan, Michel Bilello, Evan Calabrese, Errol Colak, Keyvan Farahani, Jayashree Kalpathy-Cramer, Felipe C Kitamura, Sarthak Pati, et al. The rsna-asnr-miccai brats 2021 benchmark on brain tumor segmentation and radiogenomic classification. *arXiv preprint arXiv:2107.02314*, 2021. 2, 6, 1
- [2] Jinan Bao, Hanshi Sun, Hanqiu Deng, Yinsheng He, Zhaoxiang Zhang, and Xingyu Li. Bmad: Benchmarks for medical anomaly detection. In *Proceedings of the IEEE/CVF Conference on Computer Vision and Pattern Recognition*, pages 4042–4053, 2024. 2, 1
- [3] Babak Ehteshami Bejnordi, Mitko Veta, Paul Johannes Van Diest, Bram Van Ginneken, Nico Karssemeijer, Geert Litjens, Jeroen AWM Van Der Laak, Meyke Hermesen, Quirine F Manson, Maschenka Balkenhol, et al. Diagnostic assessment of deep learning algorithms for detection of lymph node metastases in women with breast cancer. *Jama*, 318(22):2199–2210, 2017. 6, 7, 2
- [4] Paul Bergmann, Michael Fauser, David Sattlegger, and Carsten Steger. Mvtec ad—a comprehensive real-world dataset for unsupervised anomaly detection. In *Proceedings of the IEEE/CVF conference on computer vision and pattern recognition*, pages 9592–9600, 2019. 2, 6, 1
- [5] Paul Bergmann, Kilian Batzner, Michael Fauser, David Sattlegger, and Carsten Steger. Beyond dents and scratches: Logical constraints in unsupervised anomaly detection and localization. *International Journal of Computer Vision*, 130(4):947–969, 2022. 2, 3, 6, 1
- [6] Patrick Bilic, Patrick Christ, Hongwei Bran Li, Eugene Vorontsov, Avi Ben-Cohen, Georgios Kaissis, Adi Szeskin, Colin Jacobs, Gabriel Efrain Humpire Mamani, Gabriel Chartrand, et al. The liver tumor segmentation benchmark (lits). *Medical Image Analysis*, 84:102680, 2023. 2, 6
- [7] Yu Cai, Hao Chen, and Kwang-Ting Cheng. Rethinking autoencoders for medical anomaly detection from a theoretical perspective. In *International Conference on Medical Image Computing and Computer-Assisted Intervention*, pages 544–554. Springer, 2024. 3
- [8] Xuhai Chen, Yue Han, and Jiangning Zhang. April-gan: A zero-/few-shot anomaly classification and segmentation method for cvpr 2023 vand workshop challenge tracks 1&2: 1st place on zero-shot ad and 4th place on few-shot ad. *arXiv preprint arXiv:2305.17382*, 2023. 2
- [9] Choubao Ding, Guansong Pang, and Chunhua Shen. Catching both gray and black swans: Open-set supervised anomaly detection. In *Proceedings of the IEEE/CVF conference on computer vision and pattern recognition*, pages 7388–7398, 2022. 7, 8
- [10] Zhaopeng Gu, Bingke Zhu, Guibo Zhu, Yingying Chen, Hao Li, Ming Tang, and Jinqiao Wang. Filo: Zero-shot anomaly detection by fine-grained description and high-quality localization. *arXiv preprint arXiv:2404.13671*, 2024. 3
- [11] Zhaopeng Gu, Bingke Zhu, Guibo Zhu, Yingying Chen, Ming Tang, and Jinqiao Wang. Anomalygpt: Detecting industrial anomalies using large vision-language models. In *Proceedings of the AAAI Conference on Artificial Intelligence*, pages 1932–1940, 2024. 1, 2, 7
- [12] Changhee Han, Leonardo Rundo, Kohei Murao, Tomoyuki Noguchi, Yuki Shimahara, Zoltán Ádám Milacski, Saori Koshino, Evis Sala, Hideki Nakayama, and Shin’ichi Satoh. Madgan: Unsupervised medical anomaly detection gan using multiple adjacent brain mri slice reconstruction. *BMC bioinformatics*, 22:1–20, 2021. 3
- [13] Kaiming He, Xiangyu Zhang, Shaoqing Ren, and Jian Sun. Deep residual learning for image recognition. In *Proceedings of the IEEE conference on computer vision and pattern recognition*, pages 770–778, 2016. 1
- [14] Yu-Hsuan Hsieh and Shang-Hong Lai. Csad: Unsupervised component segmentation for logical anomaly detection. *arXiv preprint arXiv:2408.15628*, 2024. 2, 3
- [15] Junjie Hu, Yuanyuan Chen, and Zhang Yi. Automated segmentation of macular edema in oct using deep neural networks. *Medical image analysis*, 55:216–227, 2019. 6, 2
- [16] Chaoqin Huang, Aofan Jiang, Jinghao Feng, Ya Zhang, Xinchao Wang, and Yanfeng Wang. Adapting visual-language models for generalizable anomaly detection in medical images. In *Proceedings of the IEEE/CVF Conference on Computer Vision and Pattern Recognition*, pages 11375–11385, 2024. 2, 7, 8
- [17] Xinyu Huang, Yi-Jie Huang, Youcai Zhang, Weiwei Tian, Rui Feng, Yuejie Zhang, Yanchun Xie, Yaqian Li, and Lei

- Zhang. Open-set image tagging with multi-grained text supervision. *arXiv e-prints*, pages arXiv–2310, 2023. 2
- [18] Jeeho Hyun, Sangyun Kim, Giyoung Jeon, Seung Hwan Kim, Kyunghoon Bae, and Byung Jun Kang. Reconpatch: Contrastive patch representation learning for industrial anomaly detection. In *Proceedings of the IEEE/CVF Winter Conference on Applications of Computer Vision*, pages 2052–2061, 2024. 3
- [19] Jongheon Jeong, Yang Zou, Taewan Kim, Dongqing Zhang, Avinash Ravichandran, and Onkar Dabeer. Winclip: Zero-/few-shot anomaly classification and segmentation. In *Proceedings of the IEEE/CVF Conference on Computer Vision and Pattern Recognition*, pages 19606–19616, 2023. 1, 2, 3, 7
- [20] Daniel S Kermany, Michael Goldbaum, Wenjia Cai, Carolina CS Valentim, Huiying Liang, Sally L Baxter, Alex McKeown, Ge Yang, Xiaokang Wu, Fangbing Yan, et al. Identifying medical diagnoses and treatable diseases by image-based deep learning. *cell*, 172(5):1122–1131, 2018. 6, 2
- [21] Soopil Kim, Sion An, Philip Chikontwe, Myeongkyun Kang, Ehsan Adeli, Kilian M Pohl, and Sang Hyun Park. Few shot part segmentation reveals compositional logic for industrial anomaly detection. In *Proceedings of the AAAI Conference on Artificial Intelligence*, pages 8591–8599, 2024. 2, 3
- [22] Alexander Kirillov, Eric Mintun, Nikhila Ravi, Hanzi Mao, Chloe Rolland, Laura Gustafson, Tete Xiao, Spencer Whitehead, Alexander C Berg, Wan-Yen Lo, et al. Segment anything. In *Proceedings of the IEEE/CVF International Conference on Computer Vision*, pages 4015–4026, 2023. 2, 3, 8, 9
- [23] Bennett Landman, Zhoubing Xu, J Igelsias, Martin Styner, Thomas Langerak, and Arno Klein. Miccai multi-atlas labeling beyond the cranial vault—workshop and challenge. In *Proc. MICCAI Multi-Atlas Labeling Beyond Cranial Vault—Workshop Challenge*, page 12, 2015. 2, 6
- [24] Shilong Liu, Zhaoyang Zeng, Tianhe Ren, Feng Li, Hao Zhang, Jie Yang, Chunyuan Li, Jianwei Yang, Hang Su, Jun Zhu, et al. Grounding dino: Marrying dino with grounded pre-training for open-set object detection. *arXiv preprint arXiv:2303.05499*, 2023. 2, 8, 9
- [25] Tongkun Liu, Bing Li, Xiao Du, Bingke Jiang, Xiao Jin, Liuyi Jin, and Zhuo Zhao. Component-aware anomaly detection framework for adjustable and logical industrial visual inspection. *Advanced Engineering Informatics*, 58:102161, 2023. 2, 3, 7
- [26] Yun Peng, Xiao Lin, Nachuan Ma, Jiayuan Du, Chuangwei Liu, Chengju Liu, and Qijun Chen. Sam-lad: Segment anything model meets zero-shot logic anomaly detection. *arXiv preprint arXiv:2406.00625*, 2024. 3
- [27] Alec Radford, Jong Wook Kim, Chris Hallacy, Aditya Ramesh, Gabriel Goh, Sandhini Agarwal, Girish Sastry, Amanda Askell, Pamela Mishkin, Jack Clark, et al. Learning transferable visual models from natural language supervision. In *International conference on machine learning*, pages 8748–8763. PMLR, 2021. 1, 3
- [28] Tianhe Ren, Shilong Liu, Ailing Zeng, Jing Lin, Kunchang Li, He Cao, Jiayu Chen, Xinyu Huang, Yukang Chen, Feng Yan, et al. Grounded sam: Assembling open-world models for diverse visual tasks. *arXiv preprint arXiv:2401.14159*, 2024. 3
- [29] Karsten Roth, Latha Pemula, Joaquin Zepeda, Bernhard Schölkopf, Thomas Brox, and Peter Gehler. Towards total recall in industrial anomaly detection. In *Proceedings of the IEEE/CVF conference on computer vision and pattern recognition*, pages 14318–14328, 2022. 1, 2, 7
- [30] Olga Russakovsky, Jia Deng, Hao Su, Jonathan Krause, Sanjeev Satheesh, Sean Ma, Zhiheng Huang, Andrej Karpathy, Aditya Khosla, Michael Bernstein, Alexander C. Berg, and Li Fei-Fei. ImageNet Large Scale Visual Recognition Challenge. *International Journal of Computer Vision (IJCV)*, 115(3):211–252, 2015. 5
- [31] Yu Tian, Fengbei Liu, Guansong Pang, Yuanhong Chen, Yuyuan Liu, Johan W Verjans, Rajvinder Singh, and Gustavo Carneiro. Self-supervised pseudo multi-class pre-training for unsupervised anomaly detection and segmentation in medical images. *Medical image analysis*, 90:102930, 2023. 3
- [32] Xiaosong Wang, Yifan Peng, Le Lu, Zhiyong Lu, Mohammadhadi Bagheri, and Ronald M Summers. Chestx-ray8: Hospital-scale chest x-ray database and benchmarks on weakly-supervised classification and localization of common thorax diseases. In *Proceedings of the IEEE conference on computer vision and pattern recognition*, pages 2097–2106, 2017. 6, 2
- [33] Zifeng Wang, Zhenbang Wu, Dinesh Agarwal, and Jimeng Sun. Medclip: Contrastive learning from unpaired medical images and text. *arXiv preprint arXiv:2210.10163*, 2022. 7
- [34] Xin Xiang, Zenghui Wang, Jun Zhang, Yi Xia, Peng Chen, and Bing Wang. Agca: An adaptive graph channel attention module for steel surface defect detection. *IEEE Transactions on Instrumentation and Measurement*, 72:1–12, 2023. 6
- [35] Xincheng Yao, Ruqi Li, Jing Zhang, Jun Sun, and Chongyang Zhang. Explicit boundary guided semi-push-pull contrastive learning for supervised anomaly detection. In *Proceedings of the IEEE/CVF Conference on Computer Vision and Pattern Recognition*, pages 24490–24499, 2023. 7, 8
- [36] Zhiyuan You, Lei Cui, Yujun Shen, Kai Yang, Xin Lu, Yu Zheng, and Xinyi Le. A unified model for multi-class anomaly detection. *Advances in Neural Information Processing Systems*, 35:4571–4584, 2022. 1, 3, 7
- [37] Youcai Zhang, Xinyu Huang, Jinyu Ma, Zhaoyang Li, Zhaochuan Luo, Yanchun Xie, Yuzhuo Qin, Tong Luo, Yaqian Li, Shilong Liu, et al. Recognize anything: A strong image tagging model. In *Proceedings of the IEEE/CVF Conference on Computer Vision and Pattern Recognition*, pages 1724–1732, 2024. 3, 8, 9
- [38] Yang Zou, Jongheon Jeong, Latha Pemula, Dongqing Zhang, and Onkar Dabeer. Spot-the-difference self-supervised pre-training for anomaly detection and segmentation. In *European Conference on Computer Vision*, pages 392–408. Springer, 2022. 2, 6, 1

Appendix

A. Pseudocode Descriptions

In this section, we present Pytorch-style pseudocode for the three proposed modules: Contextual Component Clustering (C^3), Component-Aware Patch Matching (CAPM), and Graph-Enhanced Component Modeling (GECM). These pseudocode representations aim to provide readers with a clearer and more structured understanding of the implementation details for each module. Specifically, the descriptions cover key processes such as mask filtering in the C^3 module, patch matching in the CAPM module, and component feature aggregation in the GECM module. Algorithm 1, Algorithm 2, and Algorithm 3 illustrate the pseudocode for these three modules, respectively.

In the GECM module, a graph structure is employed to enhance the interaction modeling of features for each component in the image. Specifically, the features of individual components, obtained through group average pooling, are treated as nodes in the graph. The edges between these nodes are weighted based on the cosine similarity between their corresponding features, capturing the relational structure within the image.

To further model these relationships, we leverage a training-free graph attention mechanism, which facilitates the exchange of information among the graph’s nodes. In this approach, the feature of each node simultaneously serves as the Query (Q), Key (K), and Value (V). The attention mechanism is computed using the following formula:

$$Attention(Q, K, V) = norm \left(\frac{Q \cdot K^T}{\sqrt{d_k}} \right) V, \quad (14)$$

where $norm(\cdot)$ represents a normalization operation that ensures each row of the attention matrix sums to 1. A widely used normalization technique is the $softmax(\cdot)$ function, which applies an exponential scaling to emphasize relative importance among nodes. This approach allows for effective and efficient feature interaction modeling, leveraging the inherent structure of the graph without requiring additional training.

B. Dataset Details

We conduct extensive experiments on UniVAD using nine different datasets from the fields of industrial anomaly detection, logical anomaly detection, and medical anomaly detection, respectively. The following provides a detailed description of each dataset:

MVTec-AD [4] is one of the most popular datasets for industrial anomaly detection tasks, consisting of 5,354 images

Algorithm 1 Pseudocode of C^3 in a PyTorch style.

```
def C_3(image):
    # generate M_sam
    tags = RAM(image)
    M_sam = Grounded_SAM(image, tags)
    M, H, W = M_sam.shape

    # when M_sam contains only one mask
    if len(M_sam) == 1:
        area_ratio = M_sam[0].sum() / (H * W)
        if area_ratio > gamma:
            return ones_like(image)
        else:
            return M_sam

    # generate M_cluster
    image_features = image_encoder(image)
    cluster_centers = Cluster(image_features)
    # calculate feature similarity
    M_cluster = sim(
        image_features, cluster_centers
    ).argmax()

    # combine masks
    for mask in M_sam:
        label[mask] = iou(mask, M_cluster).argmax()
        M_final[label[mask]].add(mask)

    return M_final
```

across 15 different object categories. This includes 4,096 normal images and 1,258 anomalous images, with resolutions ranging from 700×700 to 1,024×1,024. The dataset covers various common industrial products, such as wooden boards, leather, metal components, and pills.

VisA [38] is a relatively recent and widely used industrial anomaly detection dataset, containing 10,821 images across 12 object categories. It includes 2,162 anomalous images, with resolutions around 1,500×1,000 pixels.

MVTec LOCO [5] is a dataset for logical anomaly detection. It is currently the largest logical anomaly detection dataset, containing 2,076 normal images and 1,568 anomalous images across 5 object categories. The anomalies in the dataset include both structural anomalies such as damage or defects, and logical anomalies such as the addition, omission, or incorrect combination of elements. The dataset provides pixel-level annotations of the anomalies.

BrainMRI [2] dataset is based on the BraTS2021 [1] dataset, one of the latest large-scale brain tumor segmentation datasets. It contains complete 3D brain volume images. The BrainMRI dataset consists of 2D slices derived from BraTS2021, with each slice image measuring 240×240 pix-

Algorithm 2 Pseudocode of CAPM in a Pytorch style.

```
def CAPM(image, normal_image, text_features):
    # get patch features
    query_feat = image_encoder(image)
    normal_feat = image_encoder(normal_image)
    query_patches = Interpolate(
        query_feat, size=image_size/patch_size
    )
    normal_patches = Interpolate(
        normal_feat, size=image_size/patch_size
    )

    # calculate score_pm
    distance_matrix = cos_distance(
        query_patches, normal_patches
    )
    score_pm = distance_matrix.min()

    # calculate score_aware and score_vl
    query_masks = C_3(image)
    normal_masks = C_3(normal_image)

    for mask, normal_mask in zip(
        query_masks, normal_masks
    ):
        distance_matrix = cos_distance(
            query_patches[mask],
            normal_patches[normal_mask]
        )
        score_capm[mask] = distance_matrix.min()

        score_vl[mask] = cos_distance(
            query_patches[mask], text_features
        )

    return (score_pm + score_aware + score_vl) / 3
```

els. The training set includes 7,500 normal samples, and the test set contains 3,715 samples, both normal and anomalous, with pixel-level anomaly annotations.

LiverCT [2] dataset is constructed from the BTCV [23] and LiTS [6] datasets. It contains 50 normal abdominal 3D CT scans from BTCV and 131 abdominal 3D CT scans, both normal and anomalous, from LiTS. The Hounsfield Unit (HU) values of the 3D scans from both datasets are converted to grayscale using the abdominal window and then cropped into 2D slices. The dataset includes 1,452 normal 2D slices for training and 1,493 2D slices, both normal and anomalous, for testing, with a resolution of 512×512 and pixel-level anomaly annotations.

RESC [15]: The Retinal Edema Segmentation Challenge (RESC) dataset is a retinal OCT dataset containing 4,297 normal images for training and 1,805 test images, both normal and anomalous. The image resolution is $512 \times 1,024$, and the dataset provides pixel-level anomaly annotations.

OCT17 [20] is another retinal OCT dataset, which includes 26,315 normal training images and 968 test images, both normal and anomalous, with a resolution of 512×496 . The dataset only provides image-level anomaly annotations.

ChestXray [32] dataset is a commonly used X-ray dataset

Algorithm 3 Pseudocode of GECM in a Pytorch style.

```
def GECM(image, normal_image):
    # extract features
    query_feat = image_encoder(image)
    normal_feat = image_encoder(normal_image)
    query_masks = C_3(image)
    normal_masks = C_3(normal_image)

    query_com_feat = {"deep": [], "geo": []}
    normal_com_feat = {"deep": [], "geo": []}

    # CFA: Component Feature Aggregator
    # GAP: Group Average Pooling
    query_com_feat["deep"] = CFA(
        GAP(query_feat, query_masks)
    )
    normal_com_feat["deep"] = CFA(
        GAP(normal_feat, normal_masks)
    )

    query_com_feat["geo"] = geo_encoder(
        query_feat, query_masks
    )
    normal_com_feat["geo"] = geo_encoder(
        normal_feat, normal_masks
    )

    # calculate scores
    for mask in query_masks:
        dis_deep[mask] = cos_distance(
            query_com_feat["deep"][mask],
            normal_com_feat["deep"][normal_masks]
        )

        dis_geo[mask] = cos_distance(
            query_com_feat["geo"][mask],
            normal_com_feat["geo"][normal_masks]
        )

    score_deep[mask] = dis_matrix_deep.min()
    score_geo[mask] = dis_matrix_geo.min()

    return (score_deep + score_geo) / 2
```

for detecting pulmonary abnormalities. It contains 8,000 normal images for training and 17,194 test images, both normal and anomalous, with a resolution of $1,024 \times 1,024$. The dataset provides image-level anomaly annotations.

HIS [2] dataset is cropped from the Camelyon16 [3] dataset, which includes 400 whole-slide images of lymph node biopsies stained with hematoxylin and eosin from breast cancer patients. The HIS dataset includes 6,091 normal image patches and 997 anomalous image patches, with a resolution of 256×256 pixels. The dataset provides image-level anomaly annotations.

C. Few-Abnormal-Shot Setting

One of the key features of UniVAD is its robust generalization capability. Without requiring any training on domain-

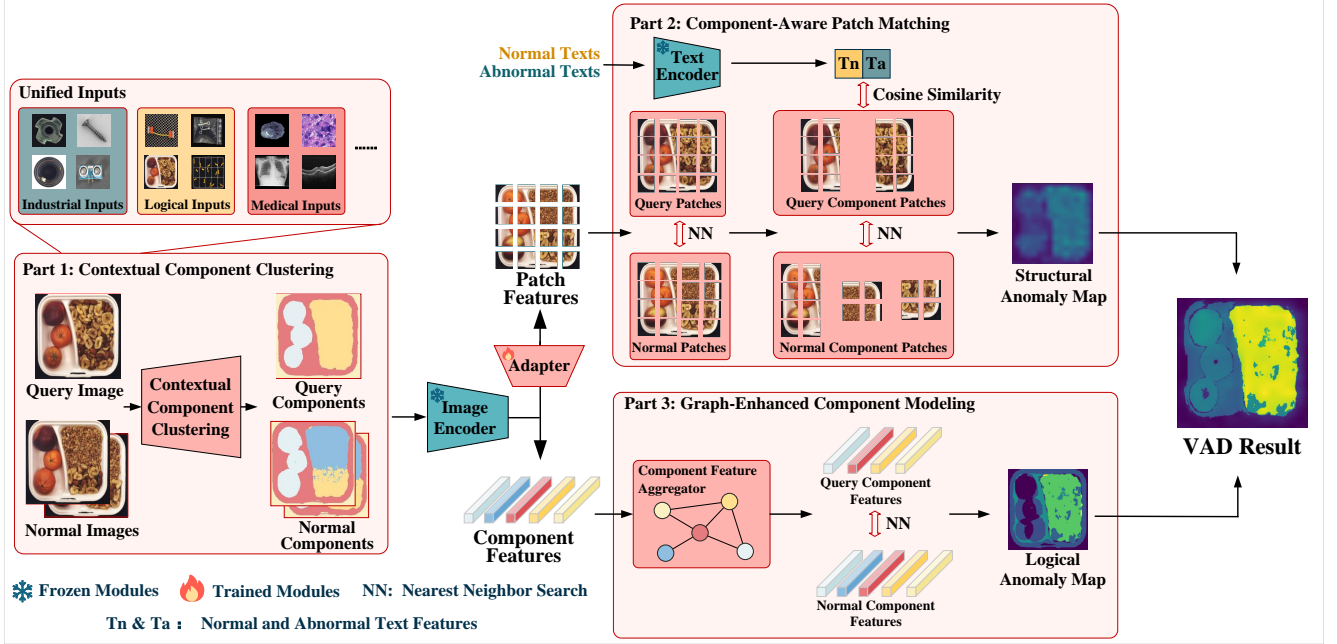


Figure 6. The overall architecture of UniVAD with a trainable adapter under few-abnormal-shot setting.

specific anomaly detection datasets, UniVAD demonstrates outstanding cross-domain anomaly detection performance by using only a minimal number of normal samples as a reference during the testing phase.

On the other hand, for scenarios demanding high-precision detection on specific domain data, we provide a domain adaptation training method. This method allows UniVAD to be fine-tuned on domain-specific datasets to achieve optimal performance for particular tasks. Such fine-tuning requires only a small number of normal and anomalous samples from the target dataset, which is referred to as the few-abnormal-shot setting.

In Section 4, in addition to the default few-normal-shot setting, we conduct experiments using the few-abnormal-shot setting and compare its performance with other methods under the same configuration. The experimental results significantly outperform existing approaches, demonstrating that UniVAD combines strong generalization capabilities with exceptional accuracy for domain-specific tasks.

Training UniVAD for domain adaptation under the few-abnormal-shot setting requires only minimal modifications to the original model: adding an adapter after the image encoder, as illustrated in Figure 6.

Regarding the adapter’s structure, we adopt bottleneck architecture, which is commonly used in computer vision and natural language processing. The specific structure, shown in Algorithm 4, consists of two linear layers, one ReLU activation layer, and one SiLU activation layer.

Algorithm 4 Adapter Module

Input: vector \mathbf{x}

Output: vector \mathbf{y}

- 1: $\mathbf{h}_1 = \text{ReLU}(\mathbf{W}_1 \mathbf{x} + \mathbf{b}_1)$
 - 2: $\mathbf{y} = \text{SiLU}(\mathbf{W}_2 \mathbf{h}_1 + \mathbf{b}_2)$
-

D. More ablation study results

In this section, we present a more detailed ablation study of the various components of our proposed method. This includes an analysis of the hierarchical levels of features extracted by the image encoder, the geometric features utilized in the GECM module, the distance metrics employed in score computation, the number of normal samples considered, and other relevant factors. Below are the detailed analyses for each aspect.

D.1. Structural Anomalies and Logical Anomalies

Each category in the MVTec LOCO dataset contains both structural and logical anomalies. UniVAD’s CAPM module and GECM module are particularly adept at detecting one type of anomaly each. In Table 7, we compare the detection performance of the CAPM and GECM modules on the MVTec LOCO dataset, highlighting the complementary collaboration between the two modules.

D.2. Normal Samples

UniVAD can perform anomaly detection and localization across various domains with only a single normal sample as

Module	MVTec LOCO Logical		MVTec LOCO Structural	
	Image-level AUC	Pixel-level AUC	Image-level AUC	Pixel-level AUC
CAPM Only	59.9	66.9	82.2	93.0
GECM Only	65.0	71.2	56.9	82.6
UniVAD	65.9	72.4	82.6	93.5

Table 7. Ablation studies of CAPM and GECM modules on MVTec LOCO datasets. The best performance results are in **bold**.

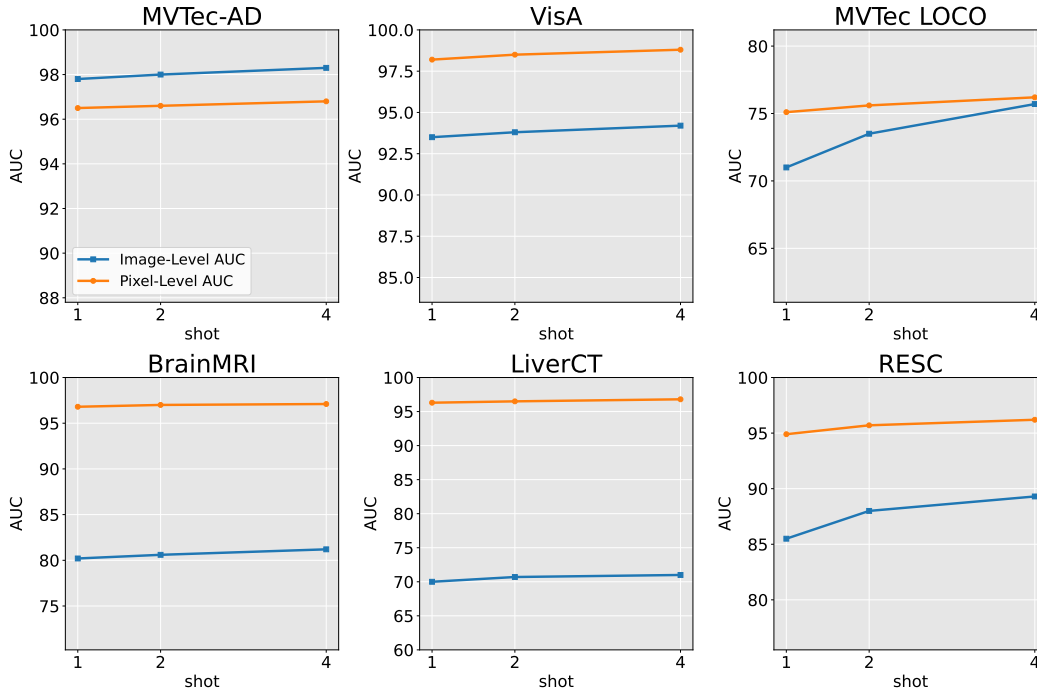


Figure 7. Experimental results of UniVAD under 1-normal-shot, 2-normal-shot, and 4-normal-shot settings.

a reference. To further evaluate its performance, we conducted experiments under settings where multiple normal samples were provided as references. Specifically, experiments were performed with 1, 2, and 4 normal samples. The experimental results under different numbers of normal samples are presented in Fig. 7. The results demonstrate that the anomaly detection performance improves progressively as the number of normal samples increases.

D.3. Multi-level Features

Numerous studies have demonstrated that image features extracted from different intermediate layers of an image encoder exhibit distinct characteristics. Shallow-layer features predominantly capture basic graphical properties such as colors and edges, while deep-layer features encapsulate more complex and abstract semantic information, including structures and textures. In UniVAD, four hierarchical feature maps are extracted from the input image, corresponding to layers 6, 12, 18, and 24 of the CLIP-ViT image encoder.

The utilization of multi-level features enhances the representation capacity for features at varying levels of abstraction within the image, thereby improving anomaly detection performance. Table 8 compares the anomaly detection performance when using features from a single layer versus employing multi-level features.

D.4. Geometric Features

In the GECM module, in addition to leveraging the deep features of each component, we also incorporate the geometric features of each component to assess logical anomalies. In UniVAD, three geometric features, *i.e.* area, color, and position, are extracted for each component and concatenated into a single vector. Table 9 presents a comparison of anomaly detection performance across different datasets when only subsets of the geometric features are utilized. The results demonstrate that each geometric feature contributes significantly to the overall performance.

Task	Dataset	Layer 6 Only	Layer 12 Only	Layer 18 Only	Layer 24 Only	UniVAD
Image-level (AUC)	MVTec-AD	96.5	96.9	97.1	96.5	97.8
	VisA	91.1	90.3	90.3	90.5	93.5
	MVTec LOCO	70.4	68.9	68.7	66.7	71.0
	BrainMRI	68.9	66.2	73.9	68.8	80.2
	LiverCT	59.0	63.4	64.4	65.5	70.0
	RESC	78.2	84.1	84.1	83.5	85.5
Pixel-level (AUC)	MVTec-AD	96.3	96.8	96.5	95.7	96.5
	VisA	95.6	97.9	97.9	97.3	98.2
	MVTec LOCO	74.7	74.6	75.5	73.2	75.1
	BrainMRI	95.3	95.8	96.9	95.4	96.8
	LiverCT	96.0	94.2	94.9	96.0	96.3
	RESC	91.5	94.3	94.6	94.0	94.9

Table 8. Ablation studies of multi-level feature utilization across different datasets. The best performance results are in **bold**.

D.5. Image Resolution

In the experiments presented in the main text, we adopt a resolution of 448×448 to remain consistent with existing mainstream anomaly detection methods. To evaluate the performance of the method in scenarios with limited computational resources, we also test UniVAD at resolutions of 224×224 and 336×336 . The experimental results shown in Fig. 8 demonstrate that, although UniVAD experiences a slight performance drop under lower-resolution settings, it still achieves satisfactory results.

D.6. Distance Calculation Method

In the CAPM and GECM modules, UniVAD calculates the distances between image patch features and component features, respectively. By default, we use cosine distance for these calculations, as described in the paper. Additionally, we evaluated UniVAD’s performance using L1 distance and L2 distance. The comparative experimental results are presented in Table 10. The results indicate that cosine distance achieves the best detection performance.

D.7. Clustering Method

In the C^3 module, we generate $M_{cluster}$ by clustering image features to filter and control the granularity of M_{sam} produced by Grounded SAM. The clustering method used in the paper is KMeans. To investigate the impact of different clustering methods on performance, we also compared Meanshift, DBSCAN, and Spectral Clustering. The comparative results, summarized in Table 11, show that anomaly detection performance is highest when using KMeans or Spectral Clustering, while Meanshift and DBSCAN yield slightly inferior results.

E. Experimental Results in More Scenarios

To further illustrate the versatility and robustness of UniVAD, we conduct experiments in various scenarios beyond standard anomaly detection datasets. These include real-world wood defect detection and crack segmentation tasks, both of which pose unique challenges and practical significance in industrial and structural inspection applications.

E.1. Real-World Wood Defect Detection

Wood, as one of the most commonly used and indispensable materials in industrial production, necessitates effective defect detection to ensure quality and reduce waste. To evaluate UniVAD’s applicability in this domain, we collected a dataset comprising real-world wood samples from production environments and applied UniVAD for defect detection. The results, visualized in Figure 9 (a), demonstrate UniVAD’s strong adaptability and generalization ability in this challenging real-world setting.

E.2. Crack Segmentation

Crack segmentation, which involves detecting and delineating cracks on surfaces such as concrete, bricks, or other structural materials, is a critical task in applications like infrastructure maintenance and surface inspection. Given the significant implications for safety and cost-efficiency, effective methods for this task are highly valued. We evaluated UniVAD on a dedicated crack segmentation dataset, assessing its performance in few-shot scenarios where limited training data are available. As shown in Figure 9 (b), UniVAD achieves excellent segmentation accuracy on the CrackVision dataset, effectively identifying cracks even on complex and textured surfaces. These results further emphasize UniVAD’s capability to address diverse and intricate anomaly detection tasks.

Task	Dataset	w/o Geo Feat.	Area Only	Area + Color	Area + Color + Position
Image-level (AUC)	MVTec-AD	97.4	97.3	97.6	97.8
	VisA	92.0	92.0	92.7	93.5
	MVTec LOCO	69.8	70.6	70.8	71.0
	BrainMRI	79.7	79.4	79.6	80.2
	LiverCT	66.4	67.9	68.9	70.0
	RESC	83.9	84.2	84.9	85.5
Pixel-level (AUC)	MVTec-AD	96.6	96.6	96.5	96.5
	VisA	98.1	98.1	98.0	98.2
	MVTec LOCO	72.4	72.1	74.9	75.1
	BrainMRI	96.8	96.8	96.8	96.8
	LiverCT	94.8	95.7	96.2	96.3
	RESC	94.4	94.4	94.7	94.9

Table 9. Ablation studies of geometric features across different datasets, Geo feat. represent components geometric features. The best performance results are in **bold**.

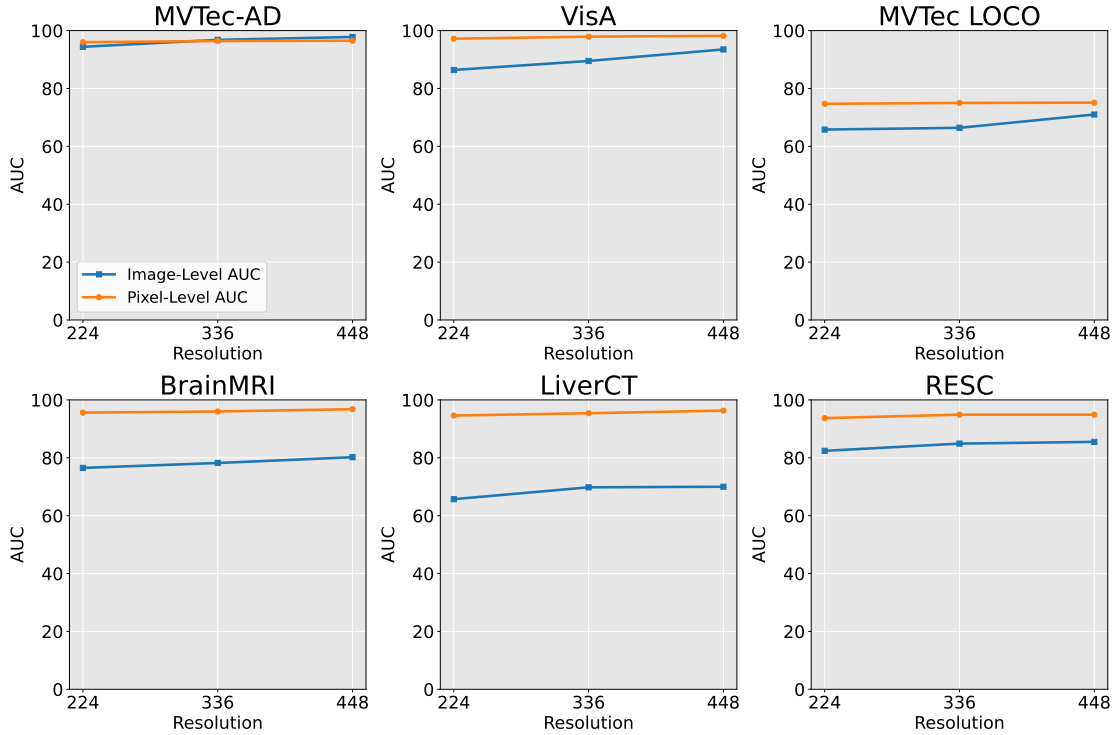


Figure 8. Experimental results of UniVAD at different resolutions.

Task	Dataset	L1 distance	L2 distance	Cosine distance
Image-level (AUC)	MVTec-AD	94.8	93.8	97.8
	VisA	87.6	87.5	93.5
	MVTec LOCO	66.4	62.1	71.0
	BrainMRI	59.3	60.2	80.2
	LiverCT	54.2	53.3	70.0
	RESC	83.4	82.5	85.5
Pixel-level (AUC)	MVTec-AD	95.3	95.7	96.5
	VisA	96.7	97.1	98.2
	MVTec LOCO	75.1	69.7	75.1
	BrainMRI	95.6	95.4	96.8
	LiverCT	95.9	96.0	96.3
	RESC	92.6	95.7	94.9

Table 10. Ablation studies of distance calculation method across different datasets. The best performance results are in **bold**.

Task	Dataset	MeanShift	DBSCAN	Spectral Clustering	Kmeans
Image-level (AUC)	MVTec-AD	96.3	97.0	97.8	97.8
	VisA	91.5	91.1	93.5	93.5
	MVTec LOCO	68.7	70.4	71.8	71.0
	BrainMRI	76.9	59.2	77.8	80.2
	LiverCT	67.7	67.7	67.9	70.0
	RESC	85.5	85.5	85.5	85.5
Pixel-level (AUC)	MVTec-AD	95.4	95.1	96.4	96.5
	VisA	96.9	97.6	98.2	98.2
	MVTec LOCO	73.1	74.0	74.5	75.1
	BrainMRI	96.6	89.2	96.6	96.8
	LiverCT	96.5	96.5	96.8	96.3
	RESC	94.9	94.9	94.9	94.9

Table 11. Ablation studies of clustering method across different datasets. The best performance results are in **bold**.

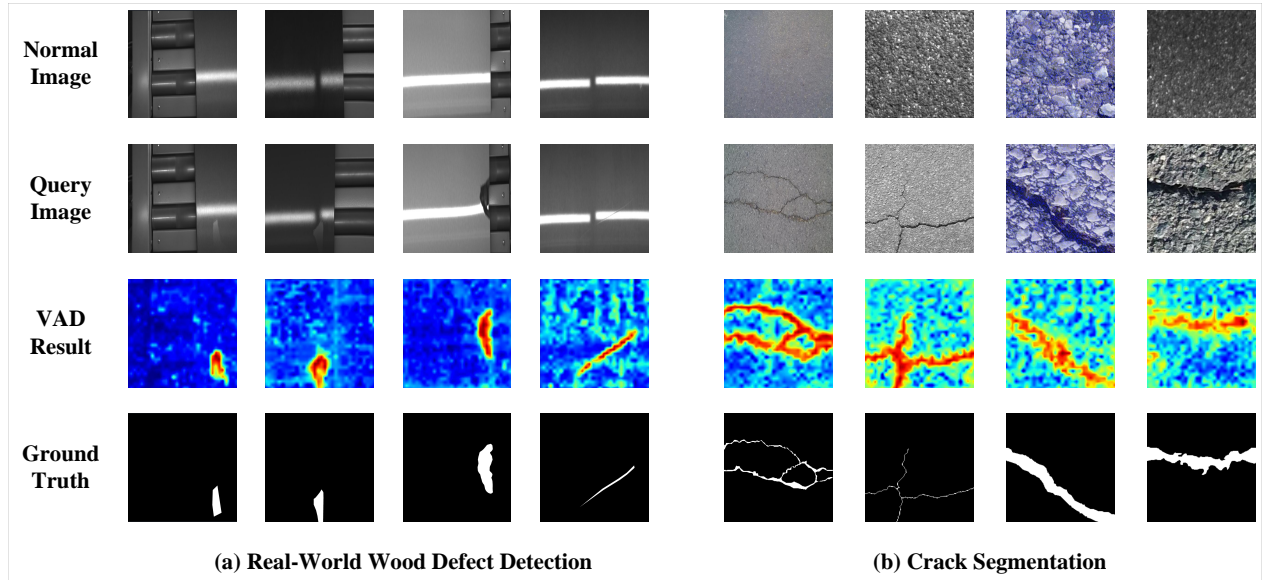


Figure 9. Visualization results in real-world wood defect detection and crack segmentation scenarios.